# Investigation of a Local Correlation-based Transition Model in a Newton-Krylov Algorithm

Michael Piotrowski*
*Institute for Aerospace Studies, University of Toronto, ON M3H 5T6*
*NASA Ames Research Center, Moffett Field, CA 94035*

David W. Zingg†
*Institute for Aerospace Studies, University of Toronto, ON M3H 5T6*

**A fully-coupled, implicit Newton-Krylov algorithm with laminar-turbulent boundary-layer transition prediction capabilities for three-dimensional external aerodynamic flows has been developed. The $\gamma$-$\tilde{Re}_{\theta t}$ Local Correlation-Based Transition Model with helicity-based crossflow correlations is modified and fully coupled to the Spalart-Allmaras turbulence model in a parallel Newton-Krylov-Schur flow solver. Deep convergence is obtained using an efficient pseudo-transient continuation time marching strategy, consisting of an approximate-Newton phase followed by an inexact-Newton phase, with source-term time stepping and exponential penalty functions used to address the strong sources and non-smooth functions introduced by the transition model. A modification to the $F_{\text{length}}$ function is introduced to improve the numerical convergence behaviour of the model. The current implementation is validated using two- and three-dimensional transition test cases, with the results obtained using the modified transition model comparing well with experiment. The elimination of discontinuities in the transition model makes it a suitable candidate for gradient-based shape optimization algorithms.**

## Nomenclature

| | |
|---|---|
| $\vec{U}$ | unit velocity vector |
| $U$ | local velocity magnitude |
| $\vec{\Omega}$ | vorticity vector |
| $\Omega$ | vorticity magnitude |
| $\Omega_{\text{streamwise}}$ | streamwise vorticity, Helicity |
| $H_{\text{crossflow}}$ | crossflow strength parameter |
| $\gamma$ | intermittency |
| $\tilde{Re}_{\theta t}$ | transported quantity of the local transition onset momentum thickness Reynolds number |
| $Re_{\theta t}$ | transition onset momentum thickness Reynolds number |
| $Re_v$ | vorticity Reynolds number |
| $d$ | minimum off-wall distance |
| $\rho$ | density |
| $\mu$ | molecular viscosity |
| $\mu_t$ | eddy viscosity |
| $u_i$ | Cartesian velocity component |
| $Tu$ | freestream turbulence intensity |
| $\lambda_\theta$ | pressure gradient parameter |
| $h$ | surface roughness height |
| $\delta$ | boundary layer thickness |
| $\theta_t$ | transition onset momentum thickness |
| $S$ | strain rate magnitude |
| $\gamma_{\text{source}}$ | largest positive source-term Jacobian eigenvalue |

*NASA Pathways Ph.D. Student, Computational Aeroscience Branch, AIAA Student member, michael.g.piotrowski@nasa.gov

†Professor, University of Toronto Distinguished Professor of Computational Aerodynamics and Sustainable Aviation, Associate Fellow AIAA, dwz@oddjob.utias.utoronto.ca

# I. Introduction

Natural-laminar-flow designs produce an increased laminar extent of the boundary layer, which results in a decrease in viscous drag [1]. This reduction in viscous drag has the potential to significantly reduce the fuel burn of transport aircraft, where it has been demonstrated to constitute approximately 50% of the total drag budget [2]. This potential has been demonstrated by NASA-supported studies which suggest the application of laminar flow control to large commercial aircraft can reduce aerodynamic drag by approximately 10% [3].

In the near term, natural laminar flow is being investigated for winglet, tail, and nacelle designs, with the Boeing 787-8 and 777X representing the first commercial applications of natural-laminar-flow nacelles to large transport aircraft, and the 737 Max aircraft exploiting laminar flow for both the nacelle and winglet designs [4]. However, in the future, the design of wing sections which exploit significant regions of laminar flow can result in more significant drag reduction. The Boeing 757 EcoDemonstrator is investigating the effect of anti-insect devices and surface coatings for the application of laminar flow on wing leading edge surfaces [5], the development of which would improve the feasibility of such designs.

Efficient high-fidelity numerical shape optimization algorithms provide the designers of next generation aircraft with a powerful tool for the development of more fuel-efficient designs [6–9]. The integration of a flow solver with transition prediction capabilities into an aerodynamic shape optimization algorithm will allow for the study of various trade-offs in the design of novel natural-laminar-flow wing configurations. In the future, the design of aircraft configurations using design tools capable of incorporating and exploiting natural laminar flow, which requires the ability to efficiently predict laminar-turbulent transition, could play a key role in reducing the environmental impact of aviation.

There are several mechanisms for boundary-layer transition. The method of transition depends greatly on the application being studied, such as flow past wings, airframes, rotor blades, and wind turbine blades, as well as the characteristics of the flow, such as Reynolds number, angle of attack, pressure gradient, and turbulence intensity. For external aerodynamic flows the two dominant mechanisms for transition result from Tollmien-Schlichting wave growth leading to natural transition and crossflow instabilities resulting from highly swept wings [10]. The effects of laminar-turbulent transition can be included in numerical simulations using various transition prediction and modeling techniques. These methods can consist of either local or non-local operations, which either attempt to predict or model the transition process depending on the fidelity of the method [11, 12].

Flow solvers based on the Reynolds-Averaged Navier-Stokes equations provide an excellent balance between accuracy, robustness, and efficiency, which make them a suitable choice for practical engineering applications that require the solution of large and complex geometries. However, turbulence models used in RANS solvers do not have the stand-alone capability to predict boundary-layer transition. In order to predict transition, one must apply a transition criterion. Reviews by Arnal et al. [11, 12] and Pasquale and Rona [13] describe the advantages and disadvantages of several approaches for coupling transition prediction criteria into RANS solvers. The most widely implemented transition prediction strategies for practical engineering applications are based on either the $e^N$ criterion or on transition onset functions.

The $e^N$ method for predicting transition is a semi-empirical approach, with the $N$-factor depending on free-stream flow conditions, based on linear stability theory. To apply the $e^N$ criterion one must first approximate the N-factor curves which represent the amplification ratios of the unstable frequencies of the disturbances in the boundary-layer. This can be achieved using stability analysis methods such as the linearized or Parabolized Stability Equations (PSE) [14], or through the use of simplified $e^N$ envelope methods, developed by Drela and Giles [15], and used by Rashad and Zingg [16] and Mayda [17], depending on the level of fidelity required in a simulation.

A boundary-layer code is often used to increase the accuracy in determining the boundary-layer edge, which is required to satisfy the requirements of the stability analysis [18]. However, recent work conducted by Rashad and Zingg [16] has demonstrated that with sufficient grid resolution, consisting of approximately 100 nodes in the boundary layer, it is possible to define the boundary-layer edge and extract the boundary-layer properties based on the RANS solution accurately, without using a boundary-layer solver. Transition models based on the $e^N$ method are able to accurately predict natural-, bypass-, and separation-induced transition. In addition, correlations for crossflow instabilities (such as the $C_1$ criterion) have been successfully combined with these approaches, with experimental validation demonstrating accurate transition prediction on transonic swept wings in three dimensions [19–21]. However, $e^N$ methods require non-local boundary-layer quantities that are not directly accessible in RANS-based CFD codes [22], and require a large infrastructure to apply the code.

In the context of the current work, the requirement that the transition model be formulated locally is significant. Modern CFD codes utilize domain decomposition and parallel computation to increase the efficiency of simulations. Non-local operations, such as integrating quantities over the boundary-layer, introduce difficulties to this process. Of

the many transition models developed for RANS-based turbulence models, two which satisfy the requirement of a fully local formulation are the empirical correlation-based $\gamma$-$\tilde{Re}_{\theta t}$ Local Correlation-based Transition Model (LCTM) developed by Langtry and Menter [23, 24], and the amplification factor transport (AFT) transition model developed by Coder and Maughmer [25, 26] and later revised by Coder [27–29].

The AFT transition model is based on the approximate envelope method for Tollmien-Schlichting wave growth, developed by Drela and Giles [15], and is able to predict natural and separation-induced transition in subsonic and transonic flow regimes. The model consists of a single transport equation for the envelope amplification factor $\tilde{n}$ with a locally-derived approximation for the boundary-layer shape factor. The transition model was originally coupled directly to the one-equation Spalart-Allmaras (SA) eddy-viscosity model [30], resulting in a two-equation coupled system [25–28]. The most recent model [29] is coupled to an additional, intermittency equation, inspired by the work of Langtry and Menter [23], resulting in a three-equation coupled system. Simulations of airfoils using the AFT model and the $\gamma$-$\tilde{Re}_{\theta t}$ LCTM coupled to the two-equation $k$-$\omega$ SST turbulence model demonstrate that the AFT transition model produces results which more accurately agree with experiment than the LCTM [25, 31]. However, at the time of this writing correlations for crossflow instabilities have not been published for the AFT transition model.

The transition model formulated by Langtry and Menter [23] is composed of two transport equations. The first is an equation for the intermittency, $\gamma$, which is used to trigger the turbulence transition process by controlling the level of turbulence in the boundary layer. The second is an equation for the transition momentum thickness Reynolds number, $\tilde{Re}_{\theta t}$, which in the free-stream is equal to the value produced by the empirical correlations, $Re_{\theta t}$, and is diffused into the boundary layer using a standard diffusion term. Transition due to crossflow instabilities represents the dominant transition mechanism for swept wings. Of the various crossflow transition models developed for the $\gamma$-$\tilde{Re}_{\theta t}$ transition model, two maintain a fully-local formulation, methods based on the local C1 criterion [32–34] and local helicity approaches [24, 35]. The local C1 approach uses the solutions of the Falkner-Skan and Cooke equations and is therefore, unlike methods based on the local helicity, only expected to work for wing-like geometries with high aspect ratios [33]. Helicity, alternatively known as the streamwise vorticity $\Omega_{\text{streamwise}}$, is the magnitude of the scalar product of the local values of the unit velocity vector, $\vec{U}$, and vorticity vector, $\vec{\Omega}$,

$$\vec{U} = \left( \frac{u}{\sqrt{u^2 + v^2 + w^2}}, \frac{v}{\sqrt{u^2 + v^2 + w^2}}, \frac{w}{\sqrt{u^2 + v^2 + w^2}} \right), \tag{1}$$

$$\vec{\Omega} = \left( \frac{\partial w}{\partial y} - \frac{\partial v}{\partial z}, \frac{\partial u}{\partial z} - \frac{\partial w}{\partial x}, \frac{\partial v}{\partial x} - \frac{\partial u}{\partial y} \right), \tag{2}$$

and can be represented using the non-dimensional crossflow strength $H_{\text{crossflow}}$ as,

$$\Omega_{\text{streamwise}} = |\vec{U} \cdot \vec{\Omega}|, \tag{3}$$

$$H_{\text{crossflow}} = \frac{y \Omega_{\text{streamwise}}}{U}. \tag{4}$$

Crossflow instability correlations based on the local helicity were initially developed by Muller and Herbst [35], with more recent correlations, which include a framework for introducing roughness effects, developed by Langtry et al. [24]. Grabe and Krumbein [33] conducted simulations using correlations based on both the C1 and helicity approaches. The C1 approach yielded more accurate results in terms of the comparison of predicted and measured transition locations on infinite swept wing flows, while the local helicity approach produced more accurate transition locations for non wing-like geometries [33].

The goal of this work is to develop a RANS-based Newton-Krylov flow solver with laminar-turbulent boundary-layer transition prediction capabilities, to be used in a high-fidelity aerodynamic shape optimization algorithm for three-dimensional external aerodynamic flows. The resulting algorithm will be used to investigate the use of natural-laminar-flow in both conventional, and unconventional aircraft configurations. Therefore, the ability to accurately predict transition on both conventional and unconventional aircraft designs, where the lifting surfaces can differ drastically from conventional wing-like geometries, is paramount.

The local helicity-based correlations developed by Muller and Herbst [35] and Langtry et al. [24] consist of an additional source term in the $\tilde{Re}_{\theta t}$ equation, which acts as a sink to reduce the value of $\tilde{Re}_{\theta t}$ in regions of significant crossflow and therefore triggers transition further upstream. While the crossflow correlations of Muller and Herbst [35] and Langtry et al. [24] are similar, the latter represents a more thoroughly validated model. Furthermore, the ability of the Langtry model to include roughness effects expands the applicability of the model. For these reasons, the transition model developed by Langtry et al. [24] was implemented in the current work.

# II. Methodology

## A. Solution Algorithm

An efficient, robust, and accurate flow solver is crucial to the performance of an optimization algorithm, as flow analysis is conducted many times over the course of the optimization process, with a variety of geometries expected. The flow solver used in the current work is a three-dimensional multi-block structured finite-difference solver developed by Hicken and Zingg [36] for the solution of the Euler equations, and extended to solve the RANS equations coupled to the one-equation SA turbulence model by Osusky and Zingg [37]. The governing equations are spatially discretized using summation-by-parts operators, with simultaneous approximation terms applied to enforce boundary conditions and inter-block coupling. To decrease the computational time required to complete a flow solution, the computational domain is decomposed into multiple blocks, resulting in multi-block structured grids, which allow for parallel computations.

A fully-coupled, implicit Newton-Krylov-Schur solution algorithm making use of a pseudo-transient continuation (PTC) strategy is applied to the set of nonlinear algebraic equations produced by the spatial discretization of the governing equations to drive the solution from an initial guess to a converged steady-state solution. The PTC strategy consists of two phases, the approximate-Newton and inexact-Newton. Globalization is achieved using the approximate-Newton phase, where an implicit Euler time marching strategy with local time linearization is applied using an approximate, analytically derived Jacobian. After the residual drops several orders of magnitude, Newton's method using the full explicit Jacobian is used to converge the system to a steady-state flow solution. The large system of linear equations generated at each iteration of the PTC strategy is solved using the GMRES linear solver [38], preconditioned using an approximate-Schur parallel preconditioner [39].

## B. Modified Local Correlation-based Transition Model

The original $\gamma$-$\tilde{Re}_{\theta t}$ formulation developed by Langtry and Menter [23] was coupled with the two-equation SST turbulence model [40]. Subsequent extensions of this model to include crossflow instabilities with correlations based on the local helicity by Grabe and Krumbein [33], Muller and Herbst [35], and Langtry et al. [24] also included this coupling. Medida and Baeder [41] modified the Langtry-Menter empirical Local Correlation-based Transition Model to be compatible with the SA turbulence model, and developed a new set of correlations validated using several test cases. Recent work demonstrated the $\gamma$-$\tilde{Re}_{\theta t}$-SA model coupled with the crossflow correlations developed by Muller and Herbst [35] was able to accurately predict transition for several three-dimensional test cases, including a swept wing, requiring only a slight modification [42]. However, their current formulation contains a function, $G_{\text{onset}}$, which requires non-local flow information.

Recent work by Shengjun et al. [43] investigated the performance of the Local Correlation-based Transition Model coupled with the SA turbulence model. Their work demonstrated that coupling the $\gamma$-$\tilde{Re}_{\theta t}$ transition model with the helicity-based crossflow correlations developed by Langtry et al. [24] to the SA turbulence model produced accurate results for two- and three-dimensional flows. However, they did not provide details of the modifications necessary for this coupling. In the current work, the $\gamma$-$\tilde{Re}_{\theta t}$ transition model is coupled to the SA turbulence model [30] using the crossflow correlations developed by Langtry et al. [24]. For compatibility, the modifications to the $R_T$ and $F_{\text{wake}}$ functions developed by Medida and Baeder [41] and Schucker [44], respectively, were implemented. In addition, adjustments to the $F_{\text{onset2}}$ and $F_{\text{onset3}}$ terms, inspired by the work of Medida and Beder [41], were applied. The modified Local Correlation-based Transition Model with helicity-based crossflow correlations coupled to the SA turbulence model, designated LCTM-SA, is presented in the following three sections.

### *1. Momentum-thickness Reynolds-number transport equation*

The transport equation for the momentum-thickness Reynolds number is defined below. The convection terms for both transition model equations have been modified to be consistent with the SA model formulation.

$$\frac{\partial \tilde{Re}_{\theta t}}{\partial t} + u_j \frac{\partial \tilde{Re}_{\theta t}}{\partial x_j} = P_{\theta t} + D_{\text{scf}} + \frac{\partial}{\partial x_j}\left[\sigma_{\theta t}(\mu + \mu_t)\frac{\partial \tilde{Re}_{\theta t}}{\partial x_j}\right] \tag{5}$$

$$P_{\theta t} = c_{\theta t}\frac{\rho}{\mathrm{t}}(Re_{\theta t} - \tilde{Re}_{\theta t})(1 - F_{\theta t}) \tag{6}$$

$$F_{\theta t} = \min\left(\max\left(F_{\text{wake}} e^{-(\frac{d}{\delta})^4}, 1 - \left(\frac{\gamma - 1/c_{e2}}{1 - 1/c_{e2}}\right)^2\right), 1\right) \tag{7}$$

$$\delta = \frac{50d\Omega}{U}\delta_{BL}; \quad \delta_{BL} = \frac{15}{2}\theta_{BL}; \quad \theta_{BL} = \frac{\tilde{Re}_{\theta t}\mu}{\rho U} \tag{8}$$

$$F_{\text{wake}} = e^{\frac{-Re_{U_{i,j}}}{6E+4}}; \quad Re_{U_{i,j}} = \frac{\rho\sqrt{\frac{dU_i}{dx_j}\frac{dU_j}{dx_i}}d^2}{\mu} \tag{9}$$

$$c_{\theta t} = 0.03; \quad \sigma_{\theta t} = 2.0 \tag{10}$$

$$\text{t} = \frac{500\mu}{\rho U^2}. \tag{11}$$

The natural and bypass transition empirical correlations are defined as follows:

$$Re_{\theta t} = \frac{\rho U\theta}{\mu} = \begin{cases} \left[1173.51 - 589.428Tu + \frac{0.2196}{Tu^2}\right]F(\lambda_\theta) & Tu \leq 1.3 \\ 331.50[Tu - 0.5658]^{-0.671}F(\lambda_\theta) & Tu > 1.3 \end{cases} \tag{12}$$

$$F(\lambda_\theta) = \begin{cases} 1 - [-12.986\lambda_\theta - 123.66\lambda_\theta^2 - 405.689\lambda_\theta^3]e^{-[\frac{Tu}{1.5}]^{1.5}} & \lambda_\theta \leq 0 \\ 1 + 0.275[1 - e^{[-35\lambda_\theta]}]e^{-[\frac{Tu}{0.5}]} & \lambda_\theta > 0 \end{cases} \tag{13}$$

$$\lambda_\theta = \frac{\rho\theta^2}{\mu}\frac{dU}{ds}; \quad U = (u^2 + v^2 + w^2)^{\frac{1}{2}} \tag{14}$$

$$\frac{dU}{ds} = \left[\left(\frac{u}{U}\right)\frac{dU}{dx} + \left(\frac{v}{U}\right)\frac{dU}{dy} + \left(\frac{w}{U}\right)\frac{dU}{dz}\right] \tag{15}$$

$$\frac{dU}{dx} = (u^2 + v^2 + w^2)^{-\frac{1}{2}} \cdot \left[u\frac{du}{dx} + v\frac{dv}{dx} + w\frac{dw}{dx}\right] \tag{16}$$

$$\frac{dU}{dy} = (u^2 + v^2 + w^2)^{-\frac{1}{2}} \cdot \left[u\frac{du}{dy} + v\frac{dv}{dy} + w\frac{dw}{dy}\right] \tag{17}$$

$$\frac{dU}{dz} = (u^2 + v^2 + w^2)^{-\frac{1}{2}} \cdot \left[u\frac{du}{dz} + v\frac{dv}{dz} + w\frac{dw}{dz}\right]. \tag{18}$$

The local turbulence intensity is not available when using the SA turbulence model. However, Suluksana et al. [45] demonstrated it can be redundant to use the local value of the turbulence intensity, $Tu$, as well as the pressure gradient parameter $\lambda_\theta$. The free-stream turbulence intensity value, $Tu_\infty$, is used throughout the domain in the current work, which is consistent with the approach taken by Medida and Baeder [41].

The helicity-based stationary crossflow correlations developed by Langtry et al. are defined below [24]:

$$D_{\text{scf}} = c_{\theta t}\frac{\rho}{\text{t}}c_{\text{crossflow}}\min(Re_{\text{scf}} - \tilde{Re}_{\theta t}, 0)(F_{\theta t2}) \tag{19}$$

$$F_{\theta t2} = \min\left(F_{\text{wake}}e^{-(\frac{d}{\delta})^4}, 1\right) \tag{20}$$

$$c_{\text{crossflow}} = 0.6 \tag{21}$$

$$Re_{\text{scf}} = \frac{\rho\left(\frac{U}{0.82}\right)\theta_t}{\mu} = -35.088\ln\left(\frac{h}{\theta_t}\right) + 319.51 + f(+\Delta H_{\text{crossflow}}) - f(-\Delta H_{\text{crossflow}}) \tag{22}$$

$$\Delta H_{\text{crossflow}} = H_{\text{crossflow}}\left(1.0 + \min\left[R_T, 0.4\right]\right) \tag{23}$$

$$+\Delta H_{\text{crossflow}} = \max(0.1066 - \Delta H_{\text{crossflow}}, 0) \tag{24}$$

$$f(+\Delta H_{\text{crossflow}}) = 6200(+\Delta H_{\text{crossflow}}) + 50000(+\Delta H_{\text{crossflow}})^2 \tag{25}$$

$$-\Delta H_{\text{crossflow}} = \max(-(0.1066 - \Delta H_{\text{crossflow}}), 0) \tag{26}$$

$$f(-\Delta H_{\text{crossflow}}) = 75\tanh\left(\frac{-\Delta H_{\text{crossflow}}}{0.0125}\right). \tag{27}$$

*2. Intermittency transport equation*

The transport equation for intermittency is:

$$\frac{\partial \gamma}{\partial t} + u_j \frac{\partial \gamma}{\partial x_j} = P_\gamma - E_\gamma + \frac{\partial}{\partial x_j}\left[\left(\mu + \frac{\mu_t}{\sigma_f}\right)\frac{\partial \gamma}{\partial x_j}\right] \tag{28}$$

$$P_\gamma = F_{\text{length}}\rho c_{a1} S\sqrt{\gamma F_{\text{onset}}}(1 - c_{e1}\gamma) \tag{29}$$

$$F_{\text{onset}} = \max(F_{\text{onset2}} - F_{\text{onset3}}, 0) \tag{30}$$

$$F_{\text{onset3}} = \max\left(2 - \left(\frac{R_T}{2.5}\right)^3, 0\right); \quad R_T = \frac{\mu_t}{\mu} \tag{31}$$

$$F_{\text{onset2}} = \min(\max(F_{\text{onset1}}, F_{\text{onset1}}^4), 4) \tag{32}$$

$$F_{\text{onset1}} = \frac{Re_\nu}{2.193 Re_{\theta c}}; \quad Re_\nu = \frac{\rho d^2}{\mu} S \tag{33}$$

$$c_{e1} = 1.0; \quad c_{a1} = 2.0; \quad \sigma_f = 1.0 \tag{34}$$

$$E_\gamma = c_{a2}\rho\Omega\gamma F_{\text{turb}}(c_{e2}\gamma - 1) \tag{35}$$

$$F_{\text{turb}} = e^{-(\frac{R_T}{4})^4} \tag{36}$$

$$c_{e2} = 50; \quad c_{a2} = 0.06. \tag{37}$$

The separation-induced transition modification is given by:

$$\gamma_{\text{sep}} = \min\left(2.0 \cdot \max\left[0, \left(\frac{Re_\nu}{3.235 Re_{\theta c}}\right) - 1\right] F_{\text{reattach}}, 2\right) F_{\theta t} \tag{38}$$

$$F_{\text{reattach}} = e^{-(\frac{R_T}{20})^4} \tag{39}$$

$$\gamma_{\text{eff}} = \max(\gamma, \gamma_{\text{sep}}). \tag{40}$$

The $F_{\text{length}}$ and $Re_{\theta c}$ correlations are as follows:

$$F_{\text{length}} = \begin{cases} 398.189 \cdot 10^{-1} + (-119.270 \cdot 10^{-4})\tilde{Re}_{\theta t} + (-132.567 \cdot 10^{-6})\tilde{Re}_{\theta t}^2 & \tilde{Re}_{\theta t} < 400 \\ 263.404 + (-123.939 \cdot 10^{-2})\tilde{Re}_{\theta t} + (194.548 \cdot 10^{-5})\tilde{Re}_{\theta t}^2 + (-101.695 \cdot 10^{-8})\tilde{Re}_{\theta t}^3 & 400 \le \tilde{Re}_{\theta t} < 596 \\ 0.5 - (\tilde{Re}_{\theta t} - 596.0) \cdot 3 \cdot 10^{-4}) & 596 \le \tilde{Re}_{\theta t} < 1200 \\ 0.3188 & 1200 \le \tilde{Re}_{\theta t} \end{cases} \tag{41}$$

$$Re_{\theta c} = \begin{cases} \tilde{Re}_{\theta t} - (396.035 \cdot 10^{-2} + (-120.656 \cdot 10^{-4})\tilde{Re}_{\theta t} + (868.230 \cdot 10^{-6})\tilde{Re}_{\theta t}^2 \\ +(-696.506 \cdot 10^{-9})\tilde{Re}_{\theta t}^3 + (174.105 \cdot 10^{-12})\tilde{Re}_{\theta t}^4) & \tilde{Re}_{\theta t} \le 1870 \\ \tilde{Re}_{\theta t} - (593.11 + 0.482(\tilde{Re}_{\theta t} - 1870.0)) & \tilde{Re}_{\theta t} > 1870. \end{cases} \tag{42}$$

Initial simulations of two- and three-dimensional test cases revealed the existing correlations, when coupled with the SA turbulence model, consistently predicted transition too far upstream. To remedy this, the $F_{\text{onset2}}$ and $F_{\text{onset3}}$ functions were modified from their original values. The results presented in Section 4 demonstrate that the current model agrees well with experimental values using this modification.

*3. Coupling to SA turbulence model*

The transition model is coupled to the SA turbulence model production term, $P_{\tilde{\nu}}$, through the following:

$$\tilde{P}_{\tilde{\nu}} = \gamma_{\text{eff}} P_{\tilde{\nu}}. \tag{43}$$

## III. Numerical Behaviour

The solution algorithm used in the current work consists of a fully-coupled, implicit Newton-Krylov-Schur algorithm. The implementation of the LCTM-SA transition model equations in such an algorithm produces substantial numerical

instabilities. The source terms in the $\gamma$-$\tilde{Re}_{\theta t}$ equations are large and highly non-linear. This leads to numerical stiffness through the presence of restrictive source-term time scales [46, 47]. Several authors [46, 48, 49] have suggested that fully-implicit approaches can lead to numerical instabilities due to the formation of Jacobians with unfavourable characteristics. More specifically, it has been demonstrated that the implicit treatment of sources can lead to unbounded solution updates, and that a modified explicit treatment of sources can improve solver performance [47]. Additionally, recent work has suggested that fully-coupled approaches may lead to reduced performance due to increased numerical stiffness [50–53]. It has been shown that relaxing the coupling between the turbulence and mean-flow, or transition and turbulence equations, can reduce this stiffness, leading to reduced computational cost [53], and improved convergence [51, 52].

However, the rate of convergence of Newton's method is closely linked to the the accuracy of the Jacobian. Neglecting terms or otherwise manipulating the Jacobian can prevent quadratic convergence [54]. An alternative approach would be to use a segregated approach in the approximate-Jacobian phase of the Newton-Krylov solver, with the linearization of the source terms neglected, and use the full Jacobian for the inexact-Newton phase. However, while this has been demonstrated to be effective for fully-turbulent simulations, the transition model equations are highly sensitive to changes in the Jacobian. Currently, the switch to the inexact-Newton phase using the fully-coupled approach results in a slight jump in the transition model residuals as we switch to the full Jacobian. Switching from a segragated approach to an exact Jacobian has been shown to destabilize the solution further. Rather than modifying the Jacobian matrix, Lian et al. [47] demonstrated that restricting the local time step based on the non-dimensional source-term number can improve solver convergence. This smooths the jump from the approximate to the inexact-Newton phase, and allows the sources to be effectively restrained while using the full Jacobian. A source-term time step restriction, based on the ideas developed by Lian et al. [47], has been implemented in the current work in order to address these instabilities.

The LCTM-SA model contains several non-smooth functions in the form of min/max operators, which negatively affect the numerical behaviour of the model. These non-smooth functions, referred to as simple kinks [55, 56], produce discontinuities in the Jacobian. This presents a problem for both the Newton-Krylov solution algorithm and the discrete-adjoint gradient-based optimization algorithm, and can lead to solution stalling. One such function, the $F_{\text{onset}}$ function, introduces simple kinks through the presence of several layers of min/max operators. Previous studies using the Langtry-Menter transition model encountered solution stalling as a result of this function and attributed to it additional stiffness introduced through the coupling of all three turbulence/transition equations, $\tilde{\nu}$, $\gamma$, $\tilde{Re}_{\theta t}$ [51, 52]. They addressed this stiffness through relaxing the coupling of the transition and turbulence model. However, in the current work this stalling has been addressed through the application of smooth approximations.

### A. Source-term time stepping

In their work, Lian et al. [47] demonstrated that an implicit scheme becomes unstable with source-term time step values greater than one. Maintaining a source-term time step less than unity can prevent unbounded solution updates, where the source-term time step is determined by the product of the eigenvalues of the source-term Jacobian with the local time step, $\lambda_{\text{source}}\Delta t$. For the current work the eigenvalues of the block diagonal source-term Jacobian are determined using a QR algorithm. For nodes where the source-term time step exceeds 0.5, the local time step is restricted as follows,

$$\text{if} \qquad \lambda_{\text{source}}\Delta t \geq 0.5, \tag{44}$$

$$\text{then} \qquad \Delta t = 0.5/\lambda_{\text{source}}, \tag{45}$$

where $\lambda_{\text{source}}$ represents the largest positive eigenvalue of the Jacobian of the source-term vector, in this case consisting of the SA and transition model source terms.

### B. Smooth min/max approximation by exponential penalty functions

Several examples of smooth approximations of non-smooth functions can be found in the literature. Rivest [57] suggested using a generalized mean-value operator, such as the $p$-mean,

$$\phi_p(x) \triangleq \frac{\left(\sum_i^n (g_i(x))^p\right)^{\frac{1}{p}}}{n}. \tag{46}$$

As $p$ approaches positive and negative infinity, we recover the maximum and minimum operators, respectively. However, this approximation only holds if $g = (g_1, ..., g_n)$ is a vector of positive real numbers, which limits its applicability. Another approach is to use an exponential penalty function [58–60], defined as

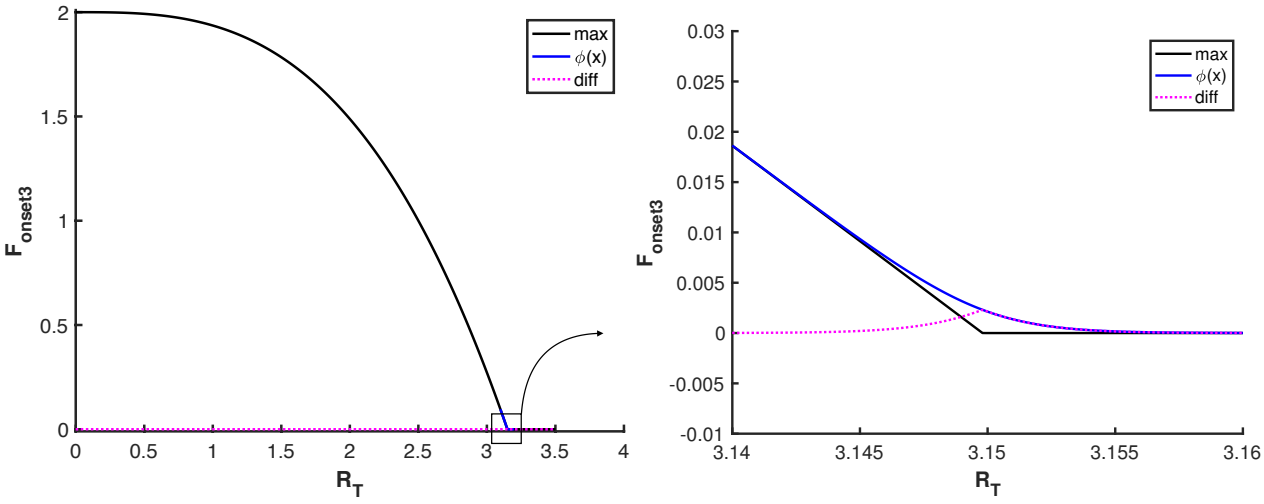


**Fig. 1 Exponential penalty function applied to $F_{\text{onset3}}$ using a $p$ value of** 300

$$\phi_p(x) \triangleq \frac{\log\left(\sum_i^n \exp(p g_i(x))\right)}{p}. \tag{47}$$

Again, as $p$ approaches positive infinity, the function produces the maximum of $g_i$, while $p$ approaching negative infinity produces the minimum. The advantage of this approach is $g = (g_1, ..., g_n)$ can be a vector of any real numbers. However, a drawback is the presence of log and exponential functions, which while producing a smooth function can increase the computational cost. This is especially true as $g_i$ approaches values close to zero. This can introduce denormalized floating point numbers which significantly slow the algorithm. To prevent this, a switch has been derived to activate the exponential penalty function only in the region near the discontinuity. The smooth approximation of a minimum/maximum operator for two functions, $g_1(x)$ and $g_2(x)$, including this switch is given as follows;

$$\text{if} \quad |g_1(x) - g_2(x)| > -\frac{\log(|p| \cdot p_{\text{mach}})}{|p|} \tag{48}$$

$$\text{then} \quad \phi_p(x) = \min \,/\, \max(g_1(x), g_2(x)) \tag{49}$$

$$\text{else} \quad \phi_p(x) = \frac{\log\left(\sum_i^n \exp(p g_i(x))\right)}{p}, \tag{50}$$

where $p_{\text{mach}}$ represents a value close to machine zero, ie. $10^{-15}$. The $F_{\text{onset3}}$ function calculated using the exponential penalty function with a $p$ value of 300, and with the switch active, is illustrated in Figure 1.

*1. $F_{length}$ approximation*

In addition to the minimum/maximum operators, the original $F_{\text{length}}$ formulation introduces simple kinks. In the current work this is avoided by approximating $F_{\text{length}}$ with a Gaussian model, and using the exponential penalty functions defined above. The new $F_{\text{length}}$ function is defined below, and presented in Figure 2,

$$t_1 = \sum_i^3 a_i \exp\left(-\left(\frac{\tilde{Re}_{\theta t} - b_i}{c_i}\right)^2\right) \tag{51}$$

$$t_2 = 0.5 - (\tilde{Re}_{\theta t} - 596.0) \cdot 3 \cdot 10^{-4} \tag{52}$$

$$t_3 = \phi_{300}(t_1, t_2) \tag{53}$$

$$F_{\text{length}} = \phi_{300}(t_3, 0.3188), \tag{54}$$

where the Gaussian model constants are defined by,

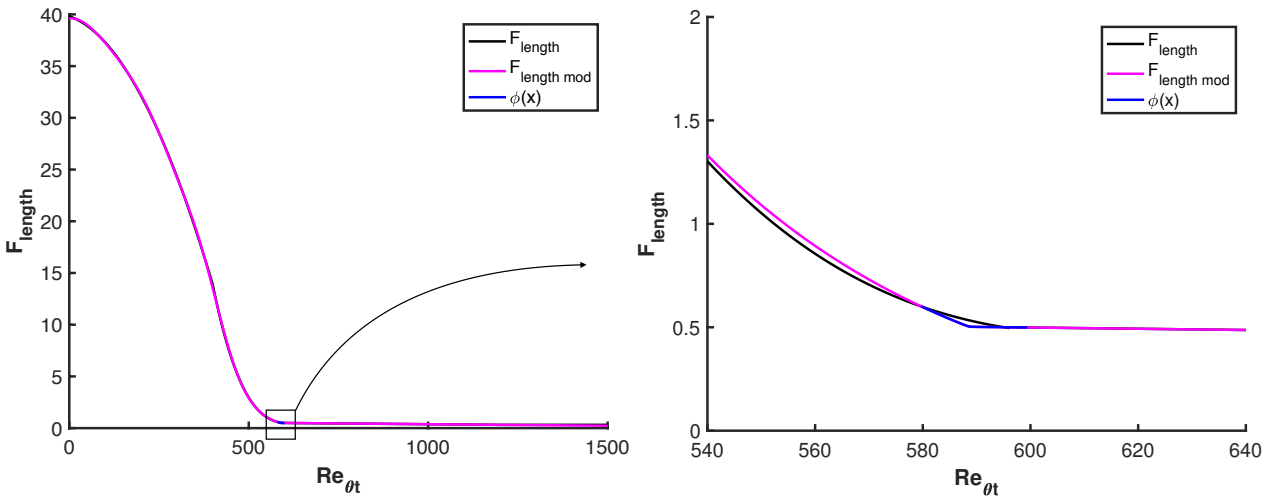


**Fig. 2 Smooth $F_{\text{length}}$ function using a $p$ value of 300**

**Table 1 Flow conditions used for the convergence study**

| | $M$ | $Re$ | $\alpha$ | $Tu$ (%) | $h$ ($\mu$m) |
|---|---|---|---|---|---|
| subsonic | 0.30 | $5.00 \times 10^6$ | 1.00 | 0.20 | 3.30 |
| transonic | 0.75 | $2.00 \times 10^7$ | 2.00 | 0.20 | 3.30 |

$$a_1 = 38.85; \quad b_1 = -13.94; \quad c_1 = 273.1 \tag{55}$$

$$a_2 = 13.00; \quad b_2 = 262.50; \quad c_2 = 159.5 \tag{56}$$

$$a_3 = 3.699; \quad b_3 = 375.90; \quad c_3 = 81.92. \tag{57}$$

Convergence plots of the LCTM-SA model with these modifications, presented in the following section, demonstrate the improved numerical behaviour of the smooth $F_{\text{length}}$ and min/max functions, while producing a negligible effect on transition location and skin friction drag.

### C. Convergence Study

Simulations of the ONERA M6 geometry [61] were conducted in order to demonstrate the effect of source-term time stepping and exponential smoothing, including the modified $F_{\text{length}}$ function, on the convergence characteristics of the LCTM-SA transition model. The ONERA M6 is a single element semispan swept, tapered wing with an aspect ratio of AR = 3.8 and a taper ratio of $\lambda = 0.562$. The leading and trailing edge sweep angles are 30° and 15.8°, respectively, resulting in a 26.7° sweep angle at the quarter chord. The cross-sectional elements of the wing are based on a symmetric airfoil using the ONERA D section perpendicular to the 40% line. Two flight conditions, which are representative of subsonic and transonic flow conditions were chosen, as presented in Table 1. Computational results were obtained using the LCTM-SA transition model on a 512 block structured mesh containing five million nodes, with a minimum off-wall spacing of $2 \times 10^{-7}$, resulting in $y^+$ values of 0.07 and 0.23 for the subsonic and transonic cases, respectively. The unscaled intermittency convergence histories are plotted versus the outer, non-linear iteration count in Figure 3.

For the subsonic cases without source-term time stepping, negative intermittency updates destabilize the solution resulting in flow solver divergence. Lian et al. demonstrated that for source-term time step values greater than unity an implicit method produces solutions with the opposite sign [47], which helps to explain this behaviour. In addition, as the solution advanced, large off-diagonal components introduced in the LCTM-SA linearization led to poor conditioning of the preconditioner, which is based on an approximate Jacobian matrix, causing the linear solver to fail. Although the transonic cases did not diverge, negative intermittency updates caused the solution to stall due to excessive variable

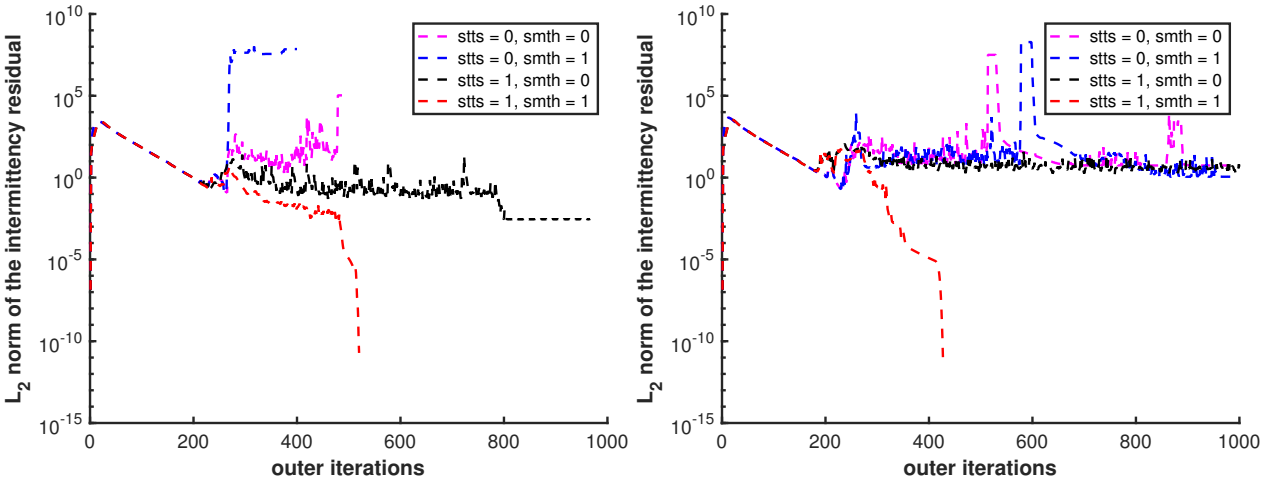


**Fig. 3 Intermittency variable convergence histories with combinations of source-term time stepping (stts) and smoothing methods (smth) active (1) and inactive (0)**

clipping to keep intermittency positive. Enabling source-term time stepping eliminated these negative intermittency updates, and improved the conditioning of the preconditioner through a reduction in the local time step.

The subsonic case without exponential smoothing failed to converge below a relative residual drop of $10^{-5}$, while the transonic case converged only three orders of magnitude. Although lift and drag converged to acceptable tolerances, for numerical shape optimization algorithms deep numerical convergence is necessary. Implementing the exponential smoothing functions, in addition to the modified $F_{\text{length}}$ function, eliminated the discontinuities in the LCTM-SA model, resulting in convergence to machine precision. The results presented in the following section use source-term time stepping and the aforementioned smoothing techniques.

## IV. Results

To validate the current implementation, including the coupling of the LCTM transition model with the SA turbulence model and the smoothing techniques described above, a range of two- and three-dimensional transition test cases were simulated. These test cases include natural and separation-induced transition and transition due to crossflow instabilities, with the results compared to experimental values.

### A. Two-Dimensional Cases

*1. NACA0012*

Experimental transition locations for the NACA0012 airfoil were obtained by Gregory and O'Reilly [62], with computational results produced by Johansen and Sorensen [63] and Mosahebi and Laurendeau [52] using an $e^N$ method and the Local Correlation-based Transition Model, respectively. Experimental results were obtained at a Reynolds number of $2.88 \times 10^6$ and Mach number of 0.16, over a range of angles of attack. A free-stream turbulence intensity value was not given for the wind tunnel. Mosahebi and Laurendeau determined the turbulence intensity as the value which produced transition locations at zero angle of attack which best matched experimental data [52], resulting in a turbulence intensity value of 0.50%. However, a Mach number of 0.10 was used in their work. A turbulence intensity of 0.20% was selected for the current work using this approach with a Mach number of 0.16 as described in experiment. Computational results obtained using the LCTM-SA model are compared with experimental results [62] in Figure 4.

The computational mesh consists of 60,320 nodes divided into 32 blocks with an off-wall spacing of $1.69 \times 10^{-6}$ chords, resulting in an average $y^+$ value of 0.18. For angles of attack less than 8° the primary transition mechanism is natural transition, with a laminar separation bubble forming and triggering transition on the upper surface of the airfoil at angles of attack of 9° and 10° [62]. The results demonstrate that the computed transition locations generated using the LCTM-SA model match well with experimental, and previously simulated results, over all angles of attack. However,

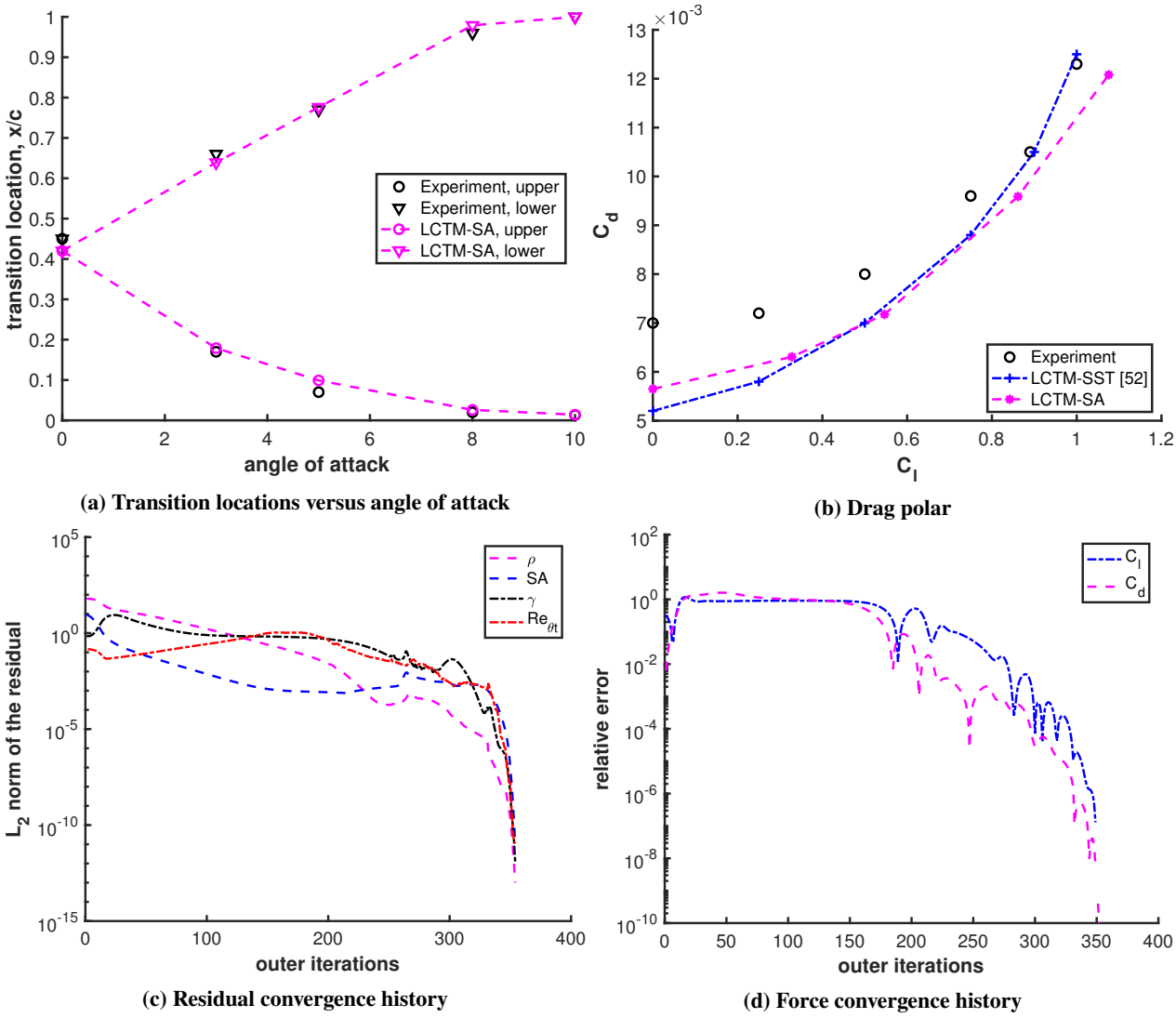


**(a) Transition locations versus angle of attack**

**(b) Drag polar**

**(c) Residual convergence history**

**(d) Force convergence history**

**Fig. 4 Experimental and computational results for transitional flow over the NACA0012 airfoil [62], where lift and drag coefficient error represents the difference between the value at each non-linear iteration and the final, converged value. Convergence behaviour is presented for the 3° angle of attack case**

the drag polar illustrates the results under-predict drag relative to experiment. This behaviour was also identified in the work of Mosahebi and Laurendeau [52] using the original LCTM model.

The convergence behaviour for the 3° angle of attack case is presented in Figures 4 (c) and (d), which illustrate the $L_2$ norm of the residuals and the error in the lift and drag coefficients relative to the converged value, respectively. Deep convergence is obtained for all angles of attack using the local source-term time stepping strategy with exponential smoothing in the fully-coupled fully-implicit algorithm.

*2. NLF0416 General Aviation Airfoil*

The NLF0416 airfoil is a natural-laminar-airfoil general aviation airfoil designed by Somers [64]. Experimental results of the NLF0416 airfoil were obtained in the low turbulence pressure tunnel at NASA Langley Research Centre [64]. Transition locations were measured for several angles of attack at a Mach number of 0.1, and a Reynolds number of $4.0 \times 10^6$. Unfortunately the turbulence intensity in the wind tunnel used for the experimental study was not specified. A value of $Tu = 0.15\%$ was assumed in order to be consistent with results obtained using the Transition Modelling and Predictive Capabilities Seminar (TCMPS) guidelines [65].

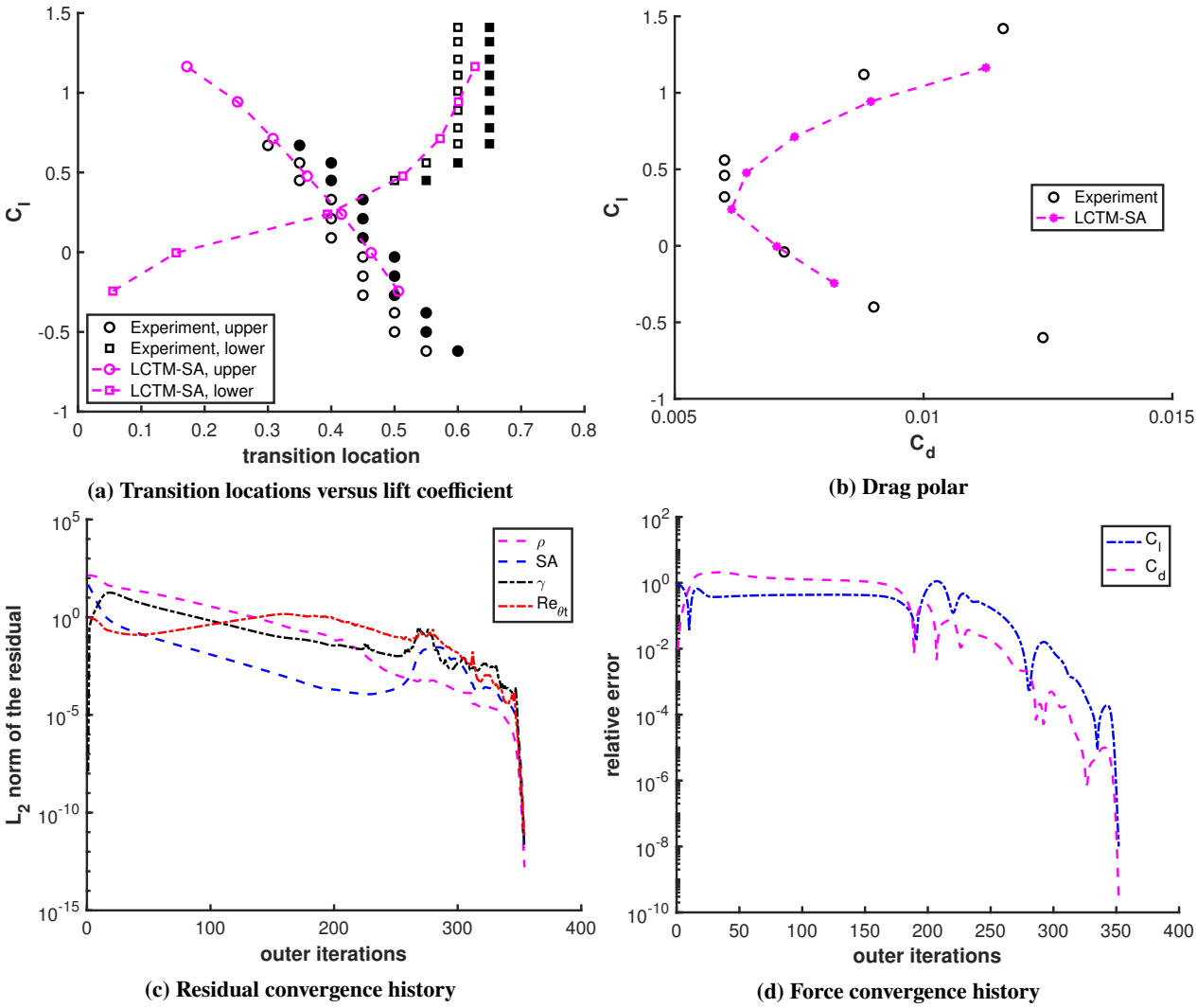


**(a) Transition locations versus lift coefficient**

**(b) Drag polar**

**(c) Residual convergence history**

**(d) Force convergence history**

**Fig. 5 Experimental and computational results for the NLF0416 airfoil, where the convergence history is presented for the 4° angle of attack case [64]**

Computational results were obtained using a mesh consisting of 137,760 nodes split into 41 blocks with an off-wall spacing of $1.38 \times 10^{-6}$ chords, resulting in an average $y^+$ value of 0.15. Results obtained using the LCTM-SA model are compared with experimental values in Figure 5. Transition locations obtained using the LCTM-SA model compare well with experimental values. The drag polar indicates that for negative angles of attack the computed values match experiment; however the LCTM-SA model begins to over-predict drag for larger angles of attack. Further validation will require a mesh-refinement study.

*3. S809 Wind Turbine Airfoil*

The S809 airfoil is a natural-laminar-flow airfoil designed by Somers [66] and studied in the low-turbulence wind tunnel of the Delft University of Technology Low Speed Laboratory. Experimental results for the S809 airfoil were obtained at a Reynolds number of $2.0 \times 10^6$ at angles of attack ranging from 0° to 9°. The free-stream turbulence intensity in the wind tunnel varied between $Tu = 0.02\%$ and $Tu = 0.04\%$. For a Reynolds number of $2.0 \times 10^6$ and an angle of attack of 0°, Somers noted the primary transition mechanism on both the upper and lower surfaces of the airfoil was separation-induced transition due to the presence of laminar separation bubbles [66]. As the angle of attack increased, the separation bubble on the upper surface decreased in length, disappearing completely at an angle of attack of 5.13°. Numerical results were obtained using a Mach number of 0.10, Reynolds number of $2.0 \times 10^6$, and a

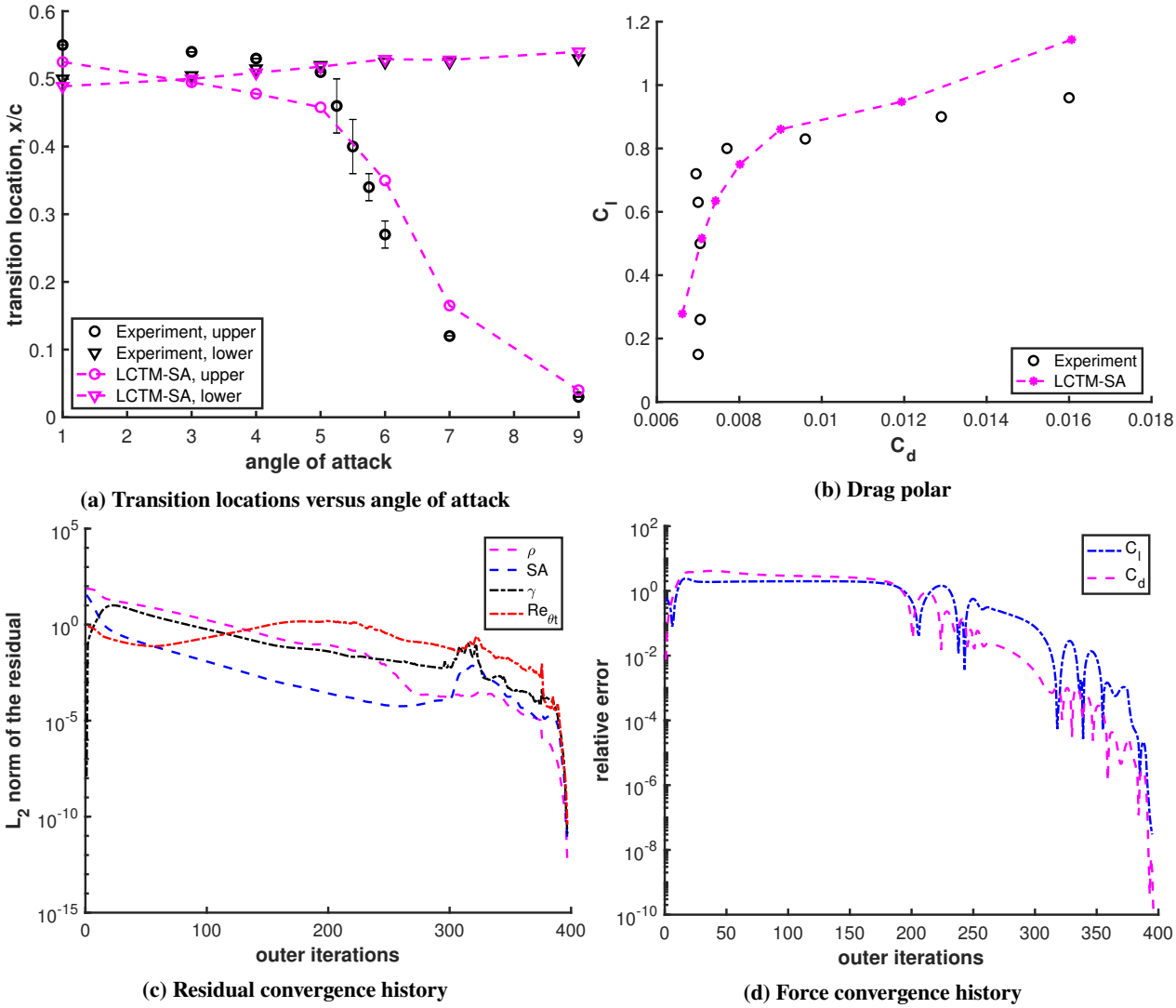


**(a) Transition locations versus angle of attack**

**(b) Drag polar**

**(c) Residual convergence history**

**(d) Force convergence history**

**Fig. 6 Experimental and computational results for the S809 airfoil, where the convergence history is presented for the 4° angle of attack case [66]**

free-stream turbulence intensity of 0.07%, as recommended by the TCMPS guidelines [65]. .

Computational results were obtained using a mesh consisting of 137,760 nodes split into 41 blocks with an off-wall spacing of $1.38 \times 10^{-6}$ chords, resulting in an average $y^+$ value of 0.10. Results obtained using the LCTM-SA model are compared with experimental results in Figure 6. As with the other results presented in this section, all cases converged to machine precision, with the exception of the 9° angle of attack case, where a large separated region on the upper leading edge surface of the airfoil caused the solution to oscillate. The plotted forces were taken as the average value of this oscillation. In their work, Denison and Pulliam [31] also encountered this large separated region when using the original LCTM model.

### B. NASA NLF2-0415 Infinite Swept Wing

The NASA NLF2-0415 Infinite Swept Wing consists of an NLF2-0415 airfoil extruded with a 45° sweep angle. Experimental measurements were obtained at an angle of attack of −4°, over a range of Mach and Reynolds numbers [67], and including a variety of surface roughness levels [68]. Transition locations were determined using the naphthalene visualization technique. Transition locations for a roughness level of 3.3$\mu$m, representing a painted surface, were obtained using the LCTM-SA model and are compared with experimental values [68] in Figure 7. The Reynolds number

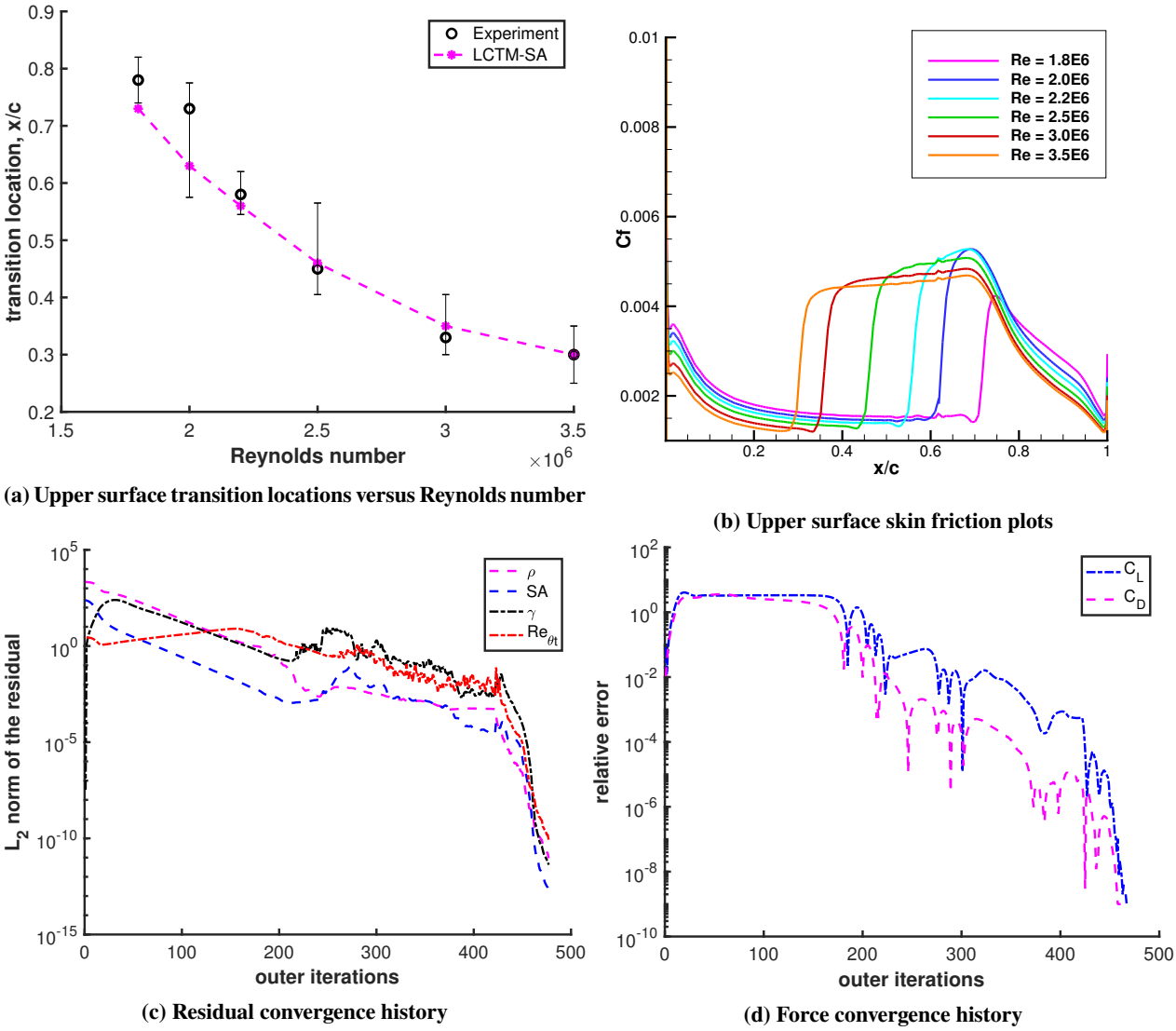


**(a) Upper surface transition locations versus Reynolds number**

**(b) Upper surface skin friction plots**

**(c) Residual convergence history**

**(d) Force convergence history**

**Fig. 7 Experimental and computational results for the NLF2-0415 infinite swept wing [68], where the convergence histories are presented for a Reynolds number of 2.2 million**

based on free-stream velocity magnitude and chord length was varied from $1.8 \times 10^6$ to $3.5 \times 10^6$. The free-stream turbulence intensity for the wind tunnel was measured as 0.20%. Transition locations are presented only for the upper surface of the wing, as experimental results are not available for the lower surface.

The computational mesh used to obtain these results consists of 9.1 million nodes split into 160 blocks, with 81,608 nodes per cross-section, and an off-wall spacing of $0.96 \times 10^{-6}$ chords, resulting in an average $y^+$ value of 0.06. Periodic boundary conditions were used to simulate the infinite swept wing. The results demonstrate that the LCTM-SA model is able to closely predict the location of transition for all cases except for the $2 \times 10^6$ Reynolds number case, where there is an error of approximately 14% between the experimental and predicted values, respectively. This error is also present in the work of Jung and Baeder [42], where they coupled a semi-local correlation-based transition model formulation with the SA model using the crossflow correlations developed by Muller and Herbst [35], and in the original model developed by Langtry et al. [24]. In the work produced by Radeztsky et al. [68], the results demonstrate that there is significant experimental error associated with this case, which helps to explain this discrepancy.

It is important to note that the choice of numerical dissipation strongly affects the accuracy of the crossflow transition model. Both the scalar dissipation model developed by Jameson et al. [69] and later refined by Pulliam [70], and the

matrix-based dissipation model developed by Swanson and Turkel [71] were investigated for this case. The scalar dissipation model drastically under predicted the crossflow strength and helicity values. This was determined to be due to the increased dissipation of the scalar dissipation model in and above the laminar boundary layer, which affected the vorticity profile within the boundary layer. For turbulent boundary layers this increased dissipation did not have a significant effect on the vorticity within the boundary layer. For the results presented in the current work, matrix-based dissipation was used with $V_l$ and $V_n$ values of 0, and a fourth-difference dissipation coefficient of 0.04.

## V. Conclusions

The $\gamma$-$\tilde{Re}_{\theta t}$ Local Correlation-based Transition Model with helicity-based crossflow correlations developed by Langtry et al. [24] has been modified to be compatible with the one-equation SA turbulence model, resulting in a new model designated LCTM-SA. The modifications maintain the fully local formulation pioneered by Langtry and Menter [23]. Deep convergence is achieved through the use of source-term time stepping and exponential smoothing functions in a fully-coupled, fully-implicit Newton-Krylov algorithm. Two- and three-dimensional test cases demonstrate that the LCTM-SA model is able to accurately predict transition due to natural, separation-, and crossflow-induced transition. The resulting model has been integrated into an aerodynamic shape optimization framework, with future work investigating the performance of the algorithm in the design of natural-laminar-flow wings.

## Acknowledgments

This work was partially funded by the NASA Transformational Tools and Technologies (TTT) and Advanced Air Transport Technology (AATT) projects, the Natural Sciences and Engineering Research Council (NSERC), the Ontario Graduate Scholarship program, and the University of Toronto. Computations were performed on the Niagara supercomputer at the SciNet HPC Consortium, a part of Compute Canada. The authors gratefully acknowledge the input and support provided by Dr. Masayuki Yano, Dr. Thomas Reist, Dr. Gaetan Kenway, Dr. Thomas Pulliam, and Dr. Cetin Kiris.

## References

[1] Green, J. E., "Civil aviation and the environment: the next frontier for the aerodynamicist," *Aeronautical Journal*, Vol. 110, No. 1110, 2006, pp. 469–486.

[2] Bushnell, D. M., "Overview of aircraft drag reduction technology," *AGARD Report 786 (Special Course on Skin Friction Drag Reduction)*, 1992.

[3] Malik, M. R., Crouch, J. D., Saric, W. S., Lin, J. C., and Whalen, E. A., "Application of Drag Reduction Techniques to Transport Aircraft," *Encyclopedia of Aerospace Engineering*, 2015.

[4] Crouch, J. D., "Boundary-Layer Transition Prediction for Laminar Flow Control," *45th AIAA Fluid Dynamics Conference*, No. AIAA-2015-2472, Dallas, TX, 2015.

[5] Week, A., "757 EcoDemo Focuses on Laminar and Active Flow," `http://aviationweek.com/technology/757-ecodemo-focuses-laminar-and-active-flow`, 2015. Accessed: 2017-05-25.

[6] Osusky, L., Buckley, H. P., Reist, T. A., and Zingg, D. W., "Drag Minimization Based on the Navier-Stokes Equations Using a Newton-Krylov Approach," *AIAA Journal*, Vol. 53, No. 6, 2015, pp. 1555–1577.

[7] Kenway, G. K. W., and Martins, J. R. R. A., "Multipoint High-Fidelity Aerostructural Optimization of a Transport Aircraft Configuration," *Journal of Aircraft*, Vol. 51, No. 1, 2014, pp. 144–160.

[8] Reist, T. A., and Zingg, D. W., "High-Fidelity Aerodynamic Shape Optimization of a Lifting-Fuselage Concept for Regional Aircraft," *Journal of Aircraft*, Vol. 54, No. 3, 2016, pp. 1085–1097.

[9] Reist, T., Zingg, D. W., Rakowitz, M., Potter, G., and Banerjee, S., "Multifidelity Optimization of Hybrid Wing-Body Aircraft with Stability and Control Requirements," *Journal of Aircraft*, Advance online publication. DOI: 10.2514/1.C034703, 2018.

[10] Reed, H. L., and Saric, W. S., "Transition mechanisms for transport aircraft," *38th Fluid Dynamics Conference and Exhibit*, No. AIAA-2008-3743, Seattle, Washington, 2008.

[11] Arnal, D., Casalis, G., and Houdeville, R., "Practical Transition Prediction Methods: Subsonic and Transonic Flows," *VKI Lecture Series: Advances in Laminar-Turbulent Transition Modeling*, 2009.

[12] Aupoix, B., Arnal, D., Bezard, H., Chaouat, B., and Chedevergne, F., "Transition and Turbulence Modeling," *AerospaceLab*, hal-01181225, 2011, pp. 1–13.

[13] Pasquale, D., Rona, A., and Garrett, S. J., "A selective review of CFD transition models," *39th AIAA Fluid Dynamics Conference*, No. AIAA-2009-3812, San Antonio, Texas, 2009.

[14] Savill, A. M., "By-pass transition using conventional closures," *Closure strategies for turbulent and transitional flows, Cambridge University Press, Cambridge*, Vol. 17, 2002, pp. 464–492.

[15] Drela, M., and Giles, M. B., "Viscous-inviscid analysis of transonic and low Reynolds number airfoils," *AIAA Journal*, Vol. 25, No. 10, 1987, pp. 1347–1355.
[16] Rashad, R., and Zingg, D. W., "Aerodynamic shape optimization for natural laminar flow using a discrete-adjoint approach," *AIAA Journal*, Vol. 54, No. 11, 2016, pp. 3321–3337.
[17] Mayda, E., "Boundary Layer Transition Prediction for Reynolds-Averaged Navier-Stokes Methods," Ph.D. thesis, University of California, Davis, 2007.
[18] Stock, H. W., "$e^N$ Transition Prediction in Three-Dimensional Boundary Layers on Inclined Prolate Spheroids," *AIAA Journal*, Vol. 44, No. 1, 2006, pp. 108–118.
[19] Moens, F., Perraud, J., Krumbein, A., Toulorge, T., Iannelli, P., and Hanifi, A., "Transition prediction and impact on a three-dimensional high-lift-wing configuration," *Journal of Aircraft*, Vol. 45, No. 5, 2008, pp. 1751–1766.
[20] Streit, T., Horstmann, H., Shraut, G., Hein, S., Fey, U., Egmai, Y., Perraud, J., Salah El Din, I., Cella, U., and Quest, J., "Complementary numerical and experimental data analysis of the ETW Telfona Pathfinder wing transition tests," *49th Aerospace Sciences Meeting and Exhibit*, No. AIAA-2011-881, Orlando, Florida, January, 2011.
[21] Shi, Y., Gross, R., Mader, C. A., and Martins, J., "Transition Prediction Based on Linear Stability Theory with the RANS Solver for Three-Dimensional Configurations," *2018 AIAA Aerospace Sciences Meeting*, No. AIAA-2018-0819, 2018.
[22] Seyfert, C., and Krumbein, A., "Evaluation of a correlation-Based Transition Model and Comparison with the $e^N$ Method," *Journal of Aircraft*, Vol. 49, No. 6, 2012, pp. 1765–1773.
[23] Langtry, R. B., and Menter, F. R., "Correlation-based transition modeling for unstructured parallelized computational fluid dynamics codes," *AIAA Journal*, Vol. 47, No. 12, 2009, pp. 2894–2906.
[24] Langtry, R. B., Sengupta, K., Yeh, D. T., and Dorgan, A. J., "Extending the $\gamma$-$\tilde{Re}_{\theta t}$ Correlation based Transition Model for Crossflow Effects," *45th AIAA Fluid Dynamics Conference*, No. AIAA-2015-2474, 2015.
[25] Coder, J. G., and Maughmer, M. D., "A CFD-Compatible Transition Model using an Amplification Factor Transport Equation," *51st AIAA Aerospace Sciences Meeting including the New Horizons Forum and Aerospace Exposition*, No. AIAA-2013-0253, 2013.
[26] Coder, J. G., and Maughmer, M. D., "Computational fluid dynamics compatible transition modeling using an amplification factor transport equation," *AIAA Journal*, Vol. 52, No. 11, 2014, pp. 2506–2512.
[27] Coder, J. G., "Enhancement of the Amplification Factor Transport Transition Modeling Framework," *55th AIAA Aerospace Sciences Meeting*, No. AIAA-2017-1709, 2017.
[28] Stefanski, D., Glasby, R., Erwin, J. T., and Coder, J. G., "Development of a Predictive Capability for Laminar-Turbulent Transition in HPCMP CREATETM-AV Kestrel Component COFFE using the Amplification Factor Transport Model," *2018 AIAA Aerospace Sciences Meeting*, No. AIAA-2018-1041, 2018.
[29] Coder, J. G., Pulliam, T. H., and Jensen, J. C., "Contributions to HiLiftPW-3 Using Structured, Overset Grid Methods," *2018 AIAA Aerospace Sciences Meeting*, No. AIAA-2018-1039, 2018.
[30] Spalart, P. R., and Allmaras, S. R., "A one equation turbulence model for aerodynamic flows," *30th AIAA Aerospace Sciences Meeting and Exhibit*, No. AIAA-092-0439, Reno, Nevada, United States 1992.
[31] Denison, M., and Pulliam, T. H., "Implementation and Assessment of the Amplification Factor Transport Laminar-Turbulent Transition Model," *2018 AIAA Aerospace Sciences Meeting*, No. AIAA-2018-3382, 2018.
[32] Choi, J. H., and Kwon, O. J., "Enhancement of a Correlation-Based Transition Turbulence Model for Simulating Crossflow Instability," *AIAA Journal*, Vol. 53, No. 10, 2015, pp. 3063–3072.
[33] Grabe, C., Shengyang, N., and Krumbein, A., "Transition Transport Modeling for the Prediction of Crossflow Transition," *34th AIAA Applied Aerodynamics Conference*, No. AIAA-2016-3572, Washington D.C., June, 2016.
[34] Xu, J. K., Bai, J. Q., Qiao, L., and Zhang, Y., "Correlation-Based Transition Transport Modeling for Simulating Crossflow Instabilities," *Journal of Applied Fluid Mechanics*, Vol. 9, No. 5, 2016, pp. 2435–2442.
[35] Muller, C., and Herbst, F., "Modelling of Crossflow-Induced Transition Based on Local Variables," *6th European Conference on Computational Fluid Dynamics (ECFD)*, 2014.
[36] Hicken, J. E., and Zingg, D. W., "Parallel Newton-Krylov solver for the Euler equations discretized using simultaneous approximation terms," *AIAA Journal*, Vol. 46, No. 11, 2008, pp. 2773–2786.
[37] Osusky, M., and Zingg, D. W., "Parallel Newton-Krylov-Schur Flow Solver for the Navier-Stokes Equations," *AIAA Journal*, Vol. 51, No. 12, 2013, pp. 2833–2851.
[38] Saad, Y., and Schultz, M. H., "GMRES: A generalized minimal residual algorithm for solving nonsymmetric linear systems," *SIAM Journal on Scientific and Statistical Computing*, Vol. 7, No. 3, 1986, pp. 856–869.
[39] Saad, Y., and Sosonkina, M., "Distributed Schur complement techniques for general sparse linear systems," *SIAM Journal of Scientific Computing*, Vol. 21, 1999, pp. 1337–1357.
[40] Menter, F. R., "Two-Equation Eddy-Viscosity Turbulence Models for Engineering Applications," *AIAA Journal*, Vol. 32, No. 8, 1994, pp. 1598–1605.
[41] Medida, S., and Baeder, J. D., "Application of the Correlation-based $\gamma$-$\tilde{Re}_{\theta t}$ Transition Model to the Spalart-Allmaras Turbulence Model," *20th AIAA Computational Fluid Dynamics Conference*, No. AIAA-2011-3979, Honolulu, HI, 2011.
[42] Jung, Y. S., and Baeder, J. D., "$\gamma$-$\tilde{Re}_{\theta t}$-SA with Crossflow Transition Model using Hamiltonian-Strand Approach," *2018 AIAA Aerospace Sciences Meeting*, No. AIAA-2018-1040, 2018.

[43] Shengjun, J., Chao, Y., and Zhifei, Y., "Integrating Stanford University Unstructured Code with Transition Model," *7th International Conference on Mechanical and Aerospace Engineering*, 2016, pp. 573–577.

[44] Schucker, J., "Development of a Three-Equation $\gamma$-$\tilde{Re}_{\theta t}$-Spalart-Allmaras Turbulence-Transition Model," Master's thesis, DLR, 2012.

[45] Suluksna, K., Dechaumphai, P., and Juntasaro, E., "Correlations for modeling transitional boundary layers under influences of freestream turbulence and pressure gradient," *International Journal of Heat and Fluid Flow*, Vol. 30, No. 1, 2009, pp. 66–75.

[46] Moryossef, Y., and Levy, Y., "Unconditionally positive implicit procedure for two-equation turbulence models: Application to k-$\omega$ turbulence models," *Journal of Computational Physics*, Vol. 220, 2006, pp. 88–108.

[47] Lian, C., Xia, G., and Merkle, C. L., "Impact of source terms on reliability of CFD algorithms," *Computers & Fluids*, Vol. 39, 2010, pp. 1909–1922.

[48] Moryossef, Y., and Levy, Y., "The unconditionally positive-convergent implicit time integration scheme for two-equation turbulence models: Revisited," *Computers & Fluids*, Vol. 38, 2009, pp. 1984–1994.

[49] Moryossef, Y., "Unconditionally stable time marching scheme for Reynolds stress models," *Journal of Computational Physics*, Vol. 276, 2014, pp. 635–664.

[50] Lee, J., and Jameson, A., "Natural-Laminar-Flow Airfoil and Wing Design by Adjoint Method and Automatic Transition Prediction," *47th AIAA Aerospace Sciences Meeting and Exhibit*, No. AIAA-2009-897, Orlando, Florida, January, 2009.

[51] Mosahebi, A., and Laurendeau, E., "Convergence Characteristics of Fully and Loosely Coupled Numerical Approaches for Transition Models," *AIAA Journal*, Vol. 53, No. 5, 2015, pp. 1399–1404.

[52] Mosahebi, A., and Laurendeau, E., "Introduction of a modified segregated numerical approach for efficient simulation of $\gamma$-$\tilde{Re}_{\theta t}$ transition model," *International Journal of Computational Fluid Dynamics*, Vol. 29, 2015, pp. 357–375.

[53] Candler, G. V., Subbareddy, P. K., and Nompelis, I., "Decoupled Implicit Method for Aerothermodynamics and Reacting Flows," *AIAA Journal*, Vol. 51, No. 5, 2013, pp. 1245–1254.

[54] Chisholm, T. T., and Zingg, D. W., "A Jacobian-free Newton-Krylov algorithm for compressible turbulent fluid flows," *Journal of Computational Physics*, Vol. 228, No. 9, 2009, pp. 3490–3507.

[55] Bertsekas, D. P., "Nondifferentiable optimization via approximation," *Mathematical Programming Study 3*, 1975, pp. 1–25.

[56] Chakraborty, A., Sinha Roy, A., and Dasgupta, B., "Non-parametric Smoothing for Gradient Methods in Non-differentiable Optimization Problems," *2016 IEEE International Conference on Systems, Man, and Cybernetics*, 2016.

[57] Rivest, R. L., "Game Tree Searching by Min/Max Approximation," *Artificial Intelligence*, Vol. 34, No. 0004-3702, 1988, pp. 77–96.

[58] Pee, E. Y., "On Solving Large-Scale Finite Minimax Problems using Exponential Smoothing," *Journal of Optimization Theory and Applications*, Vol. 148, No. 2, 2011, pp. 390–421.

[59] Polak, E., Royset, J. O., and Womersley, R. S., "Algorithms with Adaptive Smoothing for Finite Minimax Problems," *Journal of Optimization Theory and Applications*, Vol. 119, No. 3, 2003, pp. 459–484.

[60] Li, X., "An Entropy-Based Aggregate Method for Minimax Optimization," *Engineering Optimization*, Vol. 18, No. 0004-3702, 1997, pp. 277–285.

[61] Schmitt, V., Monneris, B., Dorey, G., and Capelier, C., "Etude De La Couche Limite Tridimensionnelle Sur Une Aile En Fleche," *ONERA*, Vol. Rept. 14/1713-AN, 1975.

[62] Gregory, N., and O'Reilly, C. L., "Low-Speed Aerodynamic Characteristics of NACA0012 Airfoil Section Including the Effects of Upper Surface Roughness Simulating Hoar Frost," *TR, NPL AERO Rept. 1308, Middlesex, England, UK*, 1970.

[63] Johansen, J., and Sorensen, J., "Prediction of LaminarTurbulent Transition in Airfoil Flows," *Journal of Aircraft*, Vol. 36, No. 4, 1999, pp. 731–734.

[64] Somers, D. M., "Design and experimental results for a natural-laminar-flow airfoil for general aviation applications," *NASA Langley Research Center, Hampton, VA, United States*, , No. Technical Paper 1861, 1981.

[65] Coder, J. G., "Standard Test Cases for Transition Model Verification and Validation in Computational Fluid Dynamics," *2018 AIAA Aerospace Sciences Meeting*, No. AIAA-2018-0029, 2018.

[66] Somers, D. M., "Design and experimental results for the S809 airfoil," *National Renewable Energy Laboratory, Golden, Colorado*, NRELSR-440-6918, 1989.

[67] Dagenhart, J., and Saric, W., "Crossflow stability and transition experiments in swept-wing flow," *NASA Langley Technical Report Server*, Vol. NASA/TP-1999-209344, 1999.

[68] Radeztsky, R. H., Reibert, M. S., and Saric, W. S., "Effect of Micron-Sized Roughness on Transition in Swept-Wing Flows," No. AIAA-93-0076, 1993.

[69] Jameson, A., Schmidt, W., and Turkel, E., "Numerical solution of the Euler equations by finite volume methods using Runge-Kutta time-stepping schemes," *14th Fluid and Plasma Dynamics Conference*, No. AIAA-81-1259, 1981.

[70] Pulliam, T. H., "Efficient solution methods for the Navier-Stokes equations," *Tech. rep., Lecture Notes for the von Karman Inst. for Fluid Dynamics Lecture Series: Numerical Techniques for Viscous Flow Computation in Turbomachinery Bladings*, 1986.

[71] Swanson, R. C., and Turkel, E., "On central-difference and upwind schemes," *Journal of Computational Physics*, Vol. 101, 1992, pp. 292–306.